SCIENCE ROBOTICS | RESEARCH ARTICLE

SENSORS

Solar-powered shape-changing origami microfliers

Kyle Johnson[1]†, Vicente Arroyos[1]†, Amélie Ferran[2,3], Raul Villanueva[4], Dennis Yin[4], Tilboon Elberier[4], Alberto Aliseda[2], Sawyer Fuller[1,2], Vikram Iyer[1]*, Shyamnath Gollakota[1]*

Using wind to disperse microfliers that fall like seeds and leaves can help automate large-scale sensor deployments. Here, we present battery-free microfliers that can change shape in mid-air to vary their dispersal distance. We designed origami microfliers using bistable leaf-out structures and uncovered an important property: A simple change in the shape of these origami structures causes two dramatically different falling behaviors. When unfolded and flat, the microfliers exhibit a tumbling behavior that increases lateral displacement in the wind. When folded inward, their orientation is stabilized, resulting in a downward descent that is less influenced by wind. To electronically transition between these two shapes, we designed a low-power electromagnetic actuator that produces peak forces of up to 200 millinewtons within 25 milliseconds while powered by solar cells. We fabricated a circuit directly on the folded origami structure that includes a programmable microcontroller, a Bluetooth radio, a solar power–harvesting circuit, a pressure sensor to estimate altitude, and a temperature sensor. Outdoor evaluations show that our 414-milligram origami microfliers were able to electronically change their shape mid-air, travel up to 98 meters in a light breeze, and wirelessly transmit data via Bluetooth up to 60 meters away, using only power collected from the sun.

INTRODUCTION

Many plants passively disperse biological material in the wind, such as seeds and leaves (*1*–*3*). This ability to disperse in the wind without active propulsion is useful for designing wind-dispersed microfliers (*4*, *5*). Equipped with sensors, such microfliers could automate the deployment of large-scale wireless sensor networks for environmental monitoring (*5*). These designs are much smaller and lighter than drones (*6*–*8*); however, they lack onboard actuation and thus do not have in-air control over varying their descent behavior or dispersal distance. In this work, we engineered miniaturized, battery-free, programmable microfliers that can both disperse in the wind and vary their dispersal distance through electronic actuation. The actuation can be triggered either by an onboard sensor or through wireless communication.

Achieving effective wind dispersal requires minimizing the mass of the microfliers to achieve low terminal velocities for maximum flight time. Introducing actuation and control, however, adds to the mass of the actuation mechanism and requires onboard sensing and computation for control, as well as the ability to power these components. Prior designs used fixed wing gliders (*9*) and spinning seed–inspired designs (*10*, *11*) to alter their descent behavior; however, these designs used large, power-consuming motors and servos that required heavy batteries. As a result, they were orders of magnitude larger in size and weight than our sub-gram miniaturized microfliers.

We present battery-free microfliers that are able to electronically change their shape in mid-air to alter their falling behavior and vary their dispersal distance (Fig. 1). These solar-powered miniaturized devices can be dropped from small commercial drones. They spread outward in the direction of the wind in their tumbling state. Upon reaching a programmable altitude, triggering a timer, or receiving a wireless trigger signal, these devices can use harvested power to transition to a stable state in mid-air, in which they descend with decreased lateral dispersal. Upon landing, the devices continue to harvest energy to power onboard environmental sensors and a Bluetooth radio to wirelessly transmit sensor data.

Given the limited and intermittent nature of solar harvesting, instead of continuous actuation, our microflier design used leaf-out origami based on the Miura-ori building block to produce bistable structures (*12*–*14*). These structures maintained their configuration in either of their two states without any active energy consumption.

Our work reveals an important property of leaf-out origami: These structures have different falling behaviors in their two states. Figure 2 (A and B) shows comparisons of the flat "tumbling" state, in which the structure falls chaotically, and the folded state, in which it exhibits a stable descent. A fluid analysis demonstrating the airflow around the microflier in each of its two states is shown in fig. S1. Movies S1 and S2 demonstrate that a small inward fold can emulate two distinct descent behaviors of two different leaf shapes, shown for comparison. This difference in behavior substantially changes their response to lateral wind gusts (movie S3), which can be used to vary their wind dispersal distance.

Creating a solar-powered origami microflier is challenging for three reasons. First, the structure should not transition until actively triggered. As the microflier tumbles, it encounters not only the force of the wind but also gravity acting on the mass of the payload. This imposes a trade-off between the origami design and the actuator. The structure must be stiff enough to prevent false transitions, but doing so also increases the force the actuator has to deliver, which in turn requires larger components and higher power consumption. Second, transitioning the solar-powered microflier in mid-air imposes the strict requirement that it must be completely untethered from any power source or actuation stimulus, be electronically controllable by the device itself, and produce a rapid

---

[1] Paul G. Allen School of Computer Science and Engineering, University of Washington, Seattle, WA, USA. [2] Department of Mechanical Engineering, University of Washington, Seattle, WA, USA. [3] LEGI Laboratory, Université Grenoble Alpes, CNRS, Grenoble, France. [4] Department of Electrical and Computer Engineering, University of Washington, Seattle, WA, USA.

*Corresponding author. Email: vsiyer@cs.washington.edu (V.I.); gshyam@cs.washington.edu (S.G.).

†These authors contributed equally to this work.

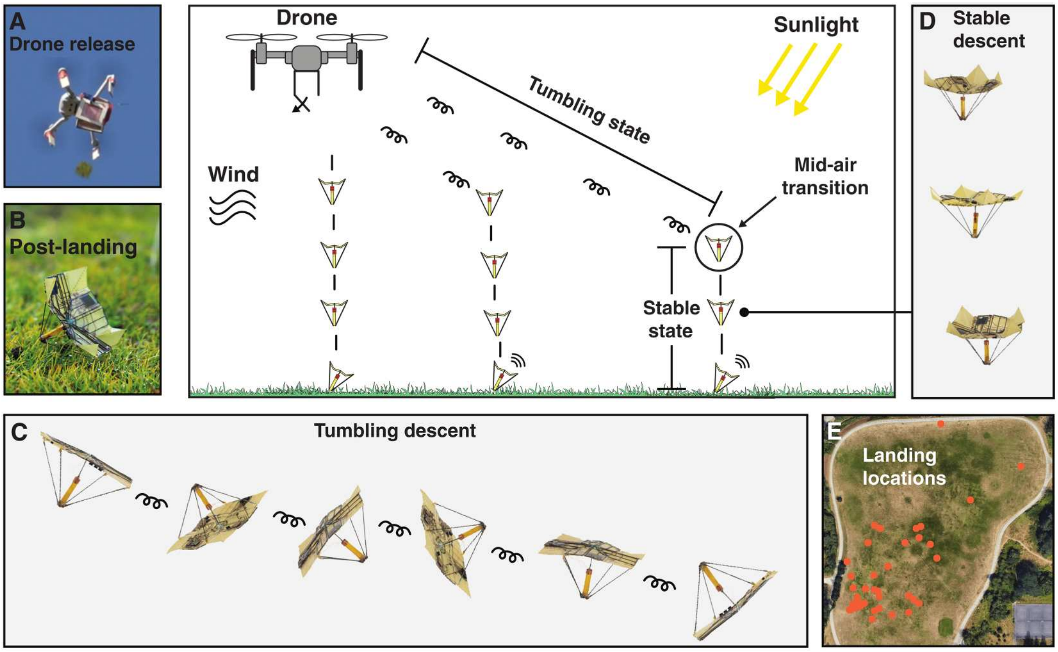

Fig. 1. Solar-powered shape-changing origami microfliers. Conceptual diagram showing origami microfliers changing their shape in mid-air to alter their falling behavior and achieve varied sensor dispersal distances. The microfliers are released from a drone (**A**) and can wirelessly transmit sensor measurements using solar power after landing (**B**). They begin falling in a flat, tumbling state (**C**) with greater lateral dispersal in the wind. The microfliers use harvested solar power to electronically transition into a folded state in mid-air after a programmable time or altitude using their onboard actuators (**D**) with stable descent and lower wind dispersal. This enables individual microfliers to achieve varying dispersal distances as shown in an aerial view showing a 100 m–by–100 m area (**E**).

response to transition before the device falls to the ground. Although origami systems that use external magnetic fields, shape memory alloys, electrothermal polymers, motors, piezoelectric actuators, or electrostatic actuators have been proposed in the literature (*15*–*26*), none of them meet our size, weight, power, and rapid response requirements. Third, this system must rapidly charge a lightweight energy storage element, such as a capacitor, up to the voltage required by the actuator and discharge a pulse of energy sufficient for transitioning. Moreover, many microcontrollers are designed for low-voltage operation to minimize power consumption and cannot tolerate the higher voltages that may be required for actuation. This requires creating separate power regulation circuits for both parts of the system and a strategy to dynamically switch between them to multiplex a single lightweight solar array.

In this article, we demonstrate that it is possible to address these challenges and build solar-powered origami microfliers that can electronically change their shape in mid-air for wind dispersal of wireless sensors. We make the following key contributions: First, we designed origami microfliers and demonstrated that small changes in their shape can dramatically change their falling behavior from chaotic tumbling to a stable descent. Further, we observed that the microfliers are more responsive to lateral wind gusts in their tumbling state, achieving as much as threefold greater dispersal distance than in their stable state. Second, we combined our origami with a low-power, bistable electromagnetic actuation mechanism compatible with solar power harvesting. This allowed our origami microflier to transition between origami states in mid-air, completely untethered. Our onboard actuator produced peak forces of up to 250 mN within 25 ms. This enabled the design of robust origami microfliers that can operate without false transition in wind speeds upward of 5 m/s. Third, we designed a solar energy harvesting circuit that can both cold start from zero charge at sunrise and harvest enough power to transition the structure in mid-air. In addition, an onboard microcontroller, a radio, and a pressure sensor enabled multiple modes of operation for triggering a transition based on time delays, altitude readings, or wireless commands. After landing, the onboard temperature and pressure sensor wirelessly transmitted data to a remote Bluetooth receiver at distances of 60 m. Last, we performed real-world deployments by dropping our sensors from drones at altitudes of 40 m and demonstrated dispersal up to distances of 98 m in a light breeze. We further showed that our 414-mg device could harvest enough energy to transition in mid-air. In addition, the devices could receive trigger signals via Bluetooth and transmit real-time sensor data as they fall for taking sensor measurements at different altitudes while landing with their solar cells facing up 87% of the time.

RESULTS

Bistable origami structure

Our objectives were to design miniaturized (sub-gram), wind-dispersed microfliers that have the ability to change their falling behavior and thereby vary their dispersal distance. One method to achieve this is to use active propulsion such as spinning rotors that can produce lift; this, however, requires substantial energy and is challenging to achieve using solar harvesting (*27*). A lower power alternative would instead be to leverage interactions with the air flowing around the microflier as it falls. In particular, the terminal velocity of a falling object is affected by its projected area and structure-dependent drag coefficient (*1*). Changing the shape of the falling

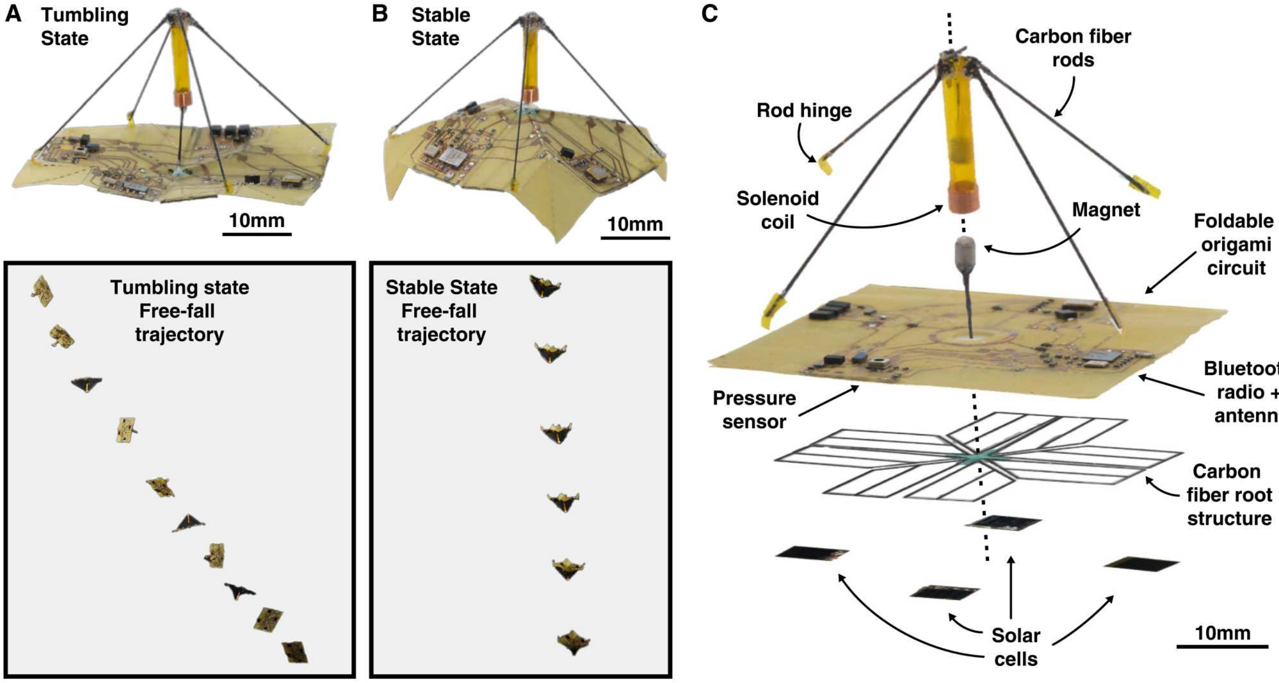

Fig. 2. Tumbling and stable states. (**A**) Origami microflier in its tumbling state. The free-fall trajectory shows sampled video frames of the flipping and lateral motion. (**B**) Origami microflier in its stable descent state. The free-fall trajectory shows stable descent and minimal lateral motion. (**C**) Disassembled view of our origami microflier showing the major components.

microflier therefore presents an alternative means of changing its descent behavior.

To create a shape change with minimal energy, we used bistable origami structures that can alternate between two different folded shapes. Specifically, we leveraged the biomimetic Miura folds that occur in leaves (*28*). The Miura-ori pattern can be tessellated as a building block for high–expansion ratio structures that produce substantial shape changes (*28*, *29*) and achieve bistable structures (*14*, *30*). In addition, the Miura-ori pattern is a form of rigid origami, meaning that the faces of the structure will not contort during folding and that deformations only occur along defined crease lines. This provides two key engineering advantages. First, energy is concentrated along the crease lines and not expended elastically deforming the faces of the structure. This minimizes the energy required to transition the structure from one state to another. Second, the lack of deformation on the faces provides stable areas in which to attach components like electronics and solar cells.

We designed our origami microfliers by combining multiple Miura-ori unit cells as shown in Fig. 3A. An individual unit cell is shown shaded gray and is composed of three distinct types of crease lines: boundary, main, and sub creases. The structure was tessellated by connecting adjacent boundary crease lines to other unit cells, with all the unit cells′ main and boundary crease lines meeting at the origin point O. Each crease is represented as either a mountain fold (protruding out of the page) or a valley fold (going into the page).

Following the rigid origami model, we assumed that all creases act like hinges between rigid and nonbendable panels (faces). Each unit cell is characterized by a central angle ($\alpha = \pi/n_{\text{cells}}$) and main crease line length ($L = OM$) parameter. The crease stiffness of our fabricated prototypes was tuned by using different materials and varying material thickness and by introducing cut patterns along the crease lines to decrease stiffness, shown in Fig. 3A. As the origami structure is folded from one state to the other, its folding stage is characterized by ψ, representing the angle between the main crease line and the Z axis extending through the center of the structure. Intuitively, this angle represents how much the main crease is folded inward.

To understand the energy requirements for changing the origami shape, we looked to prior works on leaf-out origami simulations to model the kinematics of the structure in different configurations (*13*, *14*). It has been shown that we can analyze different configurations of the leaf-out structure using the rigid origami simulation technique, where we assumed that the crease line folds are represented as torsional springs, each Miura-ori cell exhibits a single degree-of-freedom folding motion, and transformations are assumed to be uniform (*13*, *14*, *31*, *32*). A uniform transformation has all n_{cells} with equal ψ values throughout each folding stage and all mountain and valley crease assignments maintained throughout each folding stage. Using the assumptions stated above, it has been shown that we can estimate the peak energy required to transition the structure by conducting an energy analysis based on the kinematics of the leaf-out structure (*13*, *14*). Figure 3B shows the energy required to transition the structure between states for a variety of leaf-out configurations with different n_{cells}. This value represents the sum of the energy required for each fold normalized by their spring constant κ_θ (see the Supplementary Materials for details). We assumed that this constant is the same across folds because they are made from a uniform material. The normalized energy plots show that as ψ approached 0°, the flat state (the energy required to fold the structure to that angle) increased rapidly.

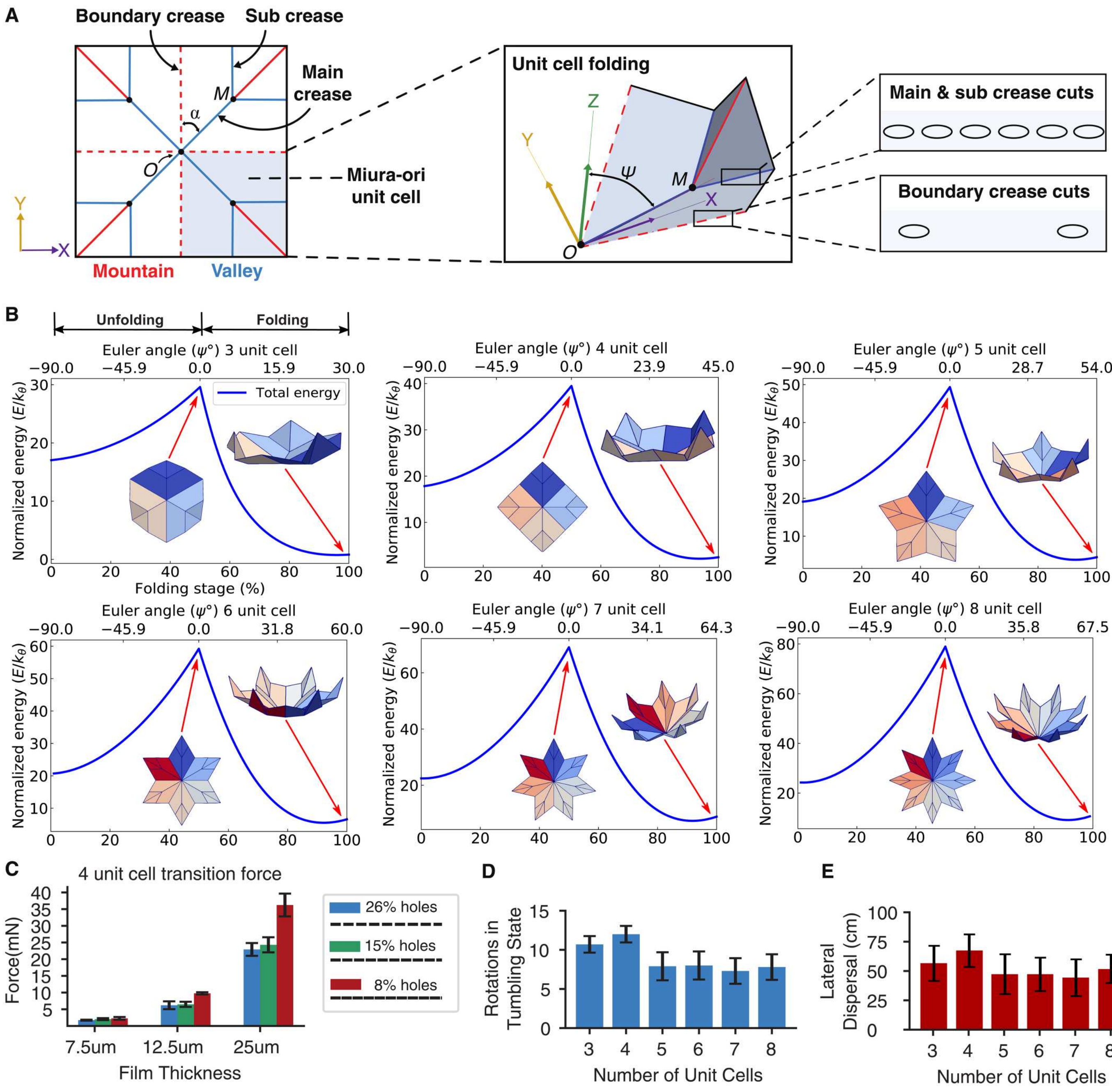

Fig. 3. Bistable origami structure. (**A**) Diagram showing the key features of the Miura-ori fold and tessellation to create structures with multiple unit cells. Sample cut patterns that add holes along the creases to tune the stiffness of origami folds are shown to the right. (**B**) Kinematics simulation showing the energy required for designs with different numbers of unit cells to transition between states. (**C**) Force required to transition a four–unit cell origami structure on different film thicknesses and various cut patterns, without electronics or actuation system ($N = 3, \pm\sigma$). (**D**) Number of flips observed when dropping designs with various numbers of unit cells in the tumbling state from 2 m ($N = 10, \pm\sigma$). (**E**) Lateral displacement when dropped from a height of 0.5 m in the tumbling state ($N \geq 10, \pm\sigma$).

Beyond this peak, the structure transitioned to its other state, and the energy rapidly decreased. Movie S4 shows how the structure folds and transitions between states. These results show that increasing the number of unit cells increased the peak energy required to transition, another parameter that can be tuned to match the ideal configuration for a given application. In this work, we optimized the n_{cells} of our leaf-out design to maximize lateral displacement for enabling dispersal in the wind over a wide area. We then tuned the material thickness and crease-cut pattern to ensure that the chosen leaf-out configuration could be transitioned given the fixed energy generated from our actuator.

Next, we evaluated how lightweight origami structures fabricated on thin films fall in each of their states. To characterize this behavior, we performed empirical measurements because of the complexities of accurately modeling the fluid-structure interactions for thin, deformable, freely falling objects. We used laser micromachining to cut out each of the simulated structures from polyimide films (see Materials and Methods for details). To tune the energy required to transition, we experimented with altering the film thickness, as well as varying the cut patterns on the boundary and subcrease lines, to vary their stiffness and therefore the force required to transition.

Specifically, we evaluated the force required to transition four unit-cell origami structures made with three different polyimide film thicknesses and boundary crease-cut patterns. We note that these experiments were performed on the bare folded film. We measured the force by placing the origami folded polyimide sheets on a precision-weight scale (Sartorius QUINTIX125D-1S) and positioning a screw-driven micromanipulator holding a flat carbon fiber plate affixed to a rod above the center of the origami. We slowly moved the carbon fiber rod and plate down to apply pressure to the origami and recorded the reading on the scale at which it transitioned. We then converted the measured mass to a force in newtons and plotted the results in Fig. 3C. The legend indicates the percentage of cut length or the percentage of holes along the crease line. A higher percentage indicates more holes along the crease and therefore lower stiffness. We performed additional characterization of how these values changed when the structure had payload, such as circuit components, on the faces in fig. S2. These experiments showed a range of forces that could be achieved by modulating the material and cut parameters. These results demonstrated the ability to achieve a variety of values to suit potential actuation strategies. During these tests, however, we observed that off-axis forces and airflow caused these thin structures to warp and violate the rigid origami design principle. To address this, we again looked to real leaves for inspiration and noted that they have rigid veins that define their structure. We emulated this by creating patterns of carbon fiber and polyethylene terephthalate (PET) as shown in Fig. 2C. We attached these carbon fiber root structures to the faces of the origami to create multilayered prototypes (see Materials and Methods and movie S4). We further found that these structures increased the force required to transition. For example, a 12.5-μm-thick leaf-out structure with 26% holes along the main and sub-creases went from requiring 6.5 mN to transition without the root structure to requiring 34 mN with the root structure.

We evaluated the microflier's resistance to false transitions in high winds by suspending the structure from a thin Kevlar thread above a fan and exposing the origami face to wind speeds up to 5 m/s. Movie S5 shows that this wind speed was strong enough to break the glue joint holding the flier in place, after which it flew into the air and landed on the ground. We note that even after experiencing this force, the structure did not falsely transition, and these results were consistent across 10 experiments averaging 7 s in duration. We further note that by tuning the material thickness and crease cuts, we could make the structure even more resilient to false transitions.

Next, we performed a series of drop tests with our origami microfliers and observed their behavior during free fall. We fabricated an array of origami designs with three to eight unit cells on 12.5-μm-thick Kapton sheets and performed drop tests ($N = 10$ trials) for each origami design in its two folded states from a height of 2 m. We recorded videos of their descent and observed that our designs reached their terminal velocity from this height.

These experiments highlighted a key difference in the behavior of the origami in its two states as shown in movies S1 to S3. When the structure was flat, it quickly began tumbling about an axis, whereas in its closed state, it exhibited a stable descent. We further observed that the tumbling state was more affected by wind gusts, giving it the potential to travel longer lateral distances during wind dispersal. The results of our drop tests comparing different origami designs in their flat and tumbling state are shown in Fig. 3 (D and E). We observed that the four–unit cell design produced a greater number of rotations as it descended compared with other designs. This is correlated with the observation that the four–unit cell design achieved greater lateral displacement from the drop location, suggesting that the momentum from this rotation caused it to move further outward from the drop location. In addition, as shown in movie S3, flipping contributed to greater lateral displacement in wind gusts. We also performed experiments analyzing falling behavior with payload and different weight distributions shown in fig. S3 and provide additional details in Supplementary Methods.

To understand the cause of this behavior, we performed particle image velocimetry (PIV) measurements to characterize the flow around and in the wake of the flier, using the setup described in fig. S1A and the Supplementary Methods (see PIV analysis). In its flat tumbling state, the flier presented sharp edges to the incoming air flow as it fell downward. We observed that the flat, tumbling configuration has a wider, highly asymmetric instantaneous wake, with higher frequency vortex shedding, which results in large aerodynamic torque with respect to the flier's center of mass. Specifically, fig. S1B shows the magnitude of the aerodynamic torque, represented by the location of the center of pressure with respect to the center of the flier, is substantially higher in the flat, tumbling state than in the stable state. The location of the center of pressure moved over a range of 10 mm at characteristic frequencies on the order of 10 Hz, causing the flier to tilt and begin tumbling. This represents the main mechanism causing the instability. Once in unstable fall, there was no aerodynamic torque to return the flier to stable fall, perpendicular to its plan. In contrast, the folded state presented beveled corners to the flow, resulting in narrower wake, as shown in the time-averaged flow velocity contours in fig. S1C. In this state, the wake vortices formed closer to the center of the flier, resulting in a more symmetric wake and lower aerodynamic torque with respect to its center of mass. Thus, the flier in the folded state was more stable: less prone to tilting its plane from falling perpendicular to gravity to aligned with gravity. Experimental methods and analysis are discussed extensively in the Supplementary Methods (see PIV analysis).

Solar-powered actuator

Creating an origami microflier that can transition in mid-air between tumbling and stable states requires careful codesign between the origami structure, actuator, and power harvesting circuit, which raises multiple design challenges. First, the structure must be robust to false transitions when it encounters the force of the wind and gravity acting on the mass of the payload. This presents a trade-off between the origami design and the actuator. The structure must be stiff enough to prevent false transitions, but doing so also increases the force the actuator has to deliver, which in turn requires larger components and higher power consumption. Second, the actuation mechanism itself must be compatible with the complex geometry of the origami structure and tolerate folding. As shown in Fig. 3A and movie S4, when the origami structure transitioned between states, the center point and creases moved up and down along the *Z* axis, whereas the borders of the structure contracted inward along the *X* and *Y* axes. This made it challenging to mount a rigid actuator on the structure at a fixed mounting point that is compliant with the origami folds. Third, the actuation mechanism must produce a rapid response to transition the device before falling to the ground. We observed that when dropped from an altitude of 40 m, our microfliers were airborne for approximately 15 s. This means that our actuator must be able to transition much faster than this to achieve our target of programmable transitions at different heights. Fourth, transitioning the structure in mid-air imposes a strict requirement that the microflier must be completely untethered from any power source or actuation stimulus and be electronically controllable by the device. To achieve this in a lightweight form factor, we used solar power harvesting; this, however, added constraints on both the total energy available and the maximum voltage and current.

Despite substantial prior work on programmable matter and robotic origami (*33*), current systems do not meet these requirements because of the well-known scaling challenges of size, weight, and power in the microrobotics community (*15*). Specifically, designs requiring external magnetic fields or heating need close proximity to the source (*16*–*18*) and cannot operate in mid-air. Other heat-actuated mechanisms like shape memory alloys (*19*, *20*) and electrothermal polymers use large amounts of energy, which would require substantially increasing size and mass to accommodate either a large solar array or a heavy battery. In addition, these actuators have slow response times and can require more than a minute to fold (*21*). Hygroscopic actuators that cause bending in response to humidity face similar drawbacks of long actuation times and are not electronically controllable (*3*, *34*). Other designs have used motors combined with thread or gearing mechanisms to achieve folding but again require large and heavy batteries and actuation mechanisms (*22*, *23*). Piezo actuators are known to be highly efficient at small scale; however, they require high voltage boost converters to drive them, which substantially increases mass and reduces efficiency (*24*, *35*). Similarly, origami designs driven by electrostatic actuators require even higher voltages of more than 1 kV (*25*). These challenges are also highlighted by recently developed small folding robots weighing approximately 10 g, and Zhakypov *et al.* (*26*) cite difficulty scaling down in size because of their use of batteries that occupy roughly half of the robot's surface area and consume 40% of its mass.

To solve these multifaceted design challenges, we analyzed different actuation modalities to identify candidates that were compatible with solar power harvesting. Each solar cell produced a maximum of 2.8 V in bright sunlight. Although this can be increased by connecting multiple cells in series, achieving hundreds or thousands of volts would require a heavy and inefficient boost converter. In addition, solar energy varies with factors like clouds and light intensity, which requires a capacitor to buffer energy. Small capacitors also cannot tolerate high voltages because of dielectric breakdown but do have low series resistance and can discharge current quickly. We therefore focused on actuators that require low voltages (<10 V) but higher currents. This suggests electromagnetic actuators or heat-based actuation. We eliminated the latter because of its slow response times and high energy requirements.

The most common electromagnetic actuators are continuously rotating motors; however, we can leverage the properties of origami to simplify our actuation to a single pulse of linear motion. As long as the force on the major crease lines exceeds the energy barrier shown in Fig. 3B, the origami structure will snap into

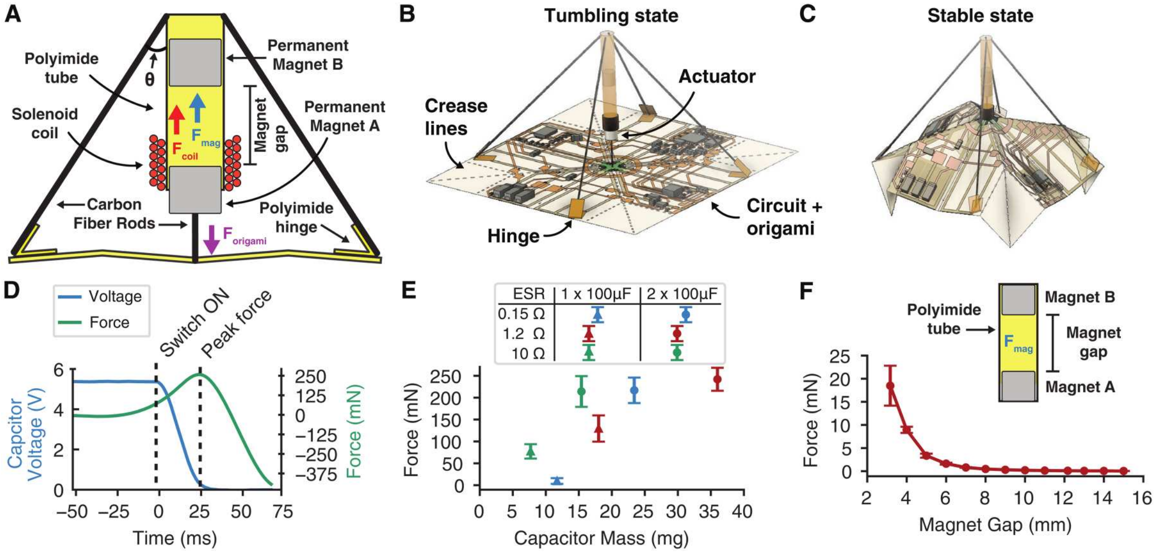

Fig. 4. Solar-powered actuator. (**A**) Diagram showing a cross-sectional view with the components of our electromagnetic solenoid actuator. (**B** and **C**) 3D models showing the actuator changing the shape of the origami from the flat (tumbling) state to the folded (stable) state. (**D**) Waveform showing the voltage of the capacitor as it discharges into the actuator and the resulting force; the actuator produces forces up to 250 mN when accelerating the magnet upward. (**E**) Actuator force achieved for capacitors of different equivalent series resistance and capacitance versus component mass (*N* = 5, ±σ). (**F**) Upward force exerted by the second magnet versus their separation gap (*N* = 4, ±σ).

its other stable state. Thus, we designed a solenoid actuator that can provide the required linear motion. At a high level, the force of a solenoid depends on the strength of the permanent magnet used and the current applied to the coil. The Lorentz force acting on the magnet can be expressed as (*36*, *37*)

$$F_{\mathrm{Lorentz}}(t) = B_{\mathrm{radial}}[x(t)]I_{\mathrm{coil}}(t)l_{\mathrm{coil}}n_{\mathrm{turns}} \quad (1)$$

The term B_{radial} is the magnetic field experienced by the coil, which varies with the position of the magnet $x(t)$; I_{coil} denotes the current applied to the coil; l_{coil} refers to the length of the coil; and n_{turns} is the number of windings. This lends itself well to our capacitor-based energy storage scheme because low series resistance capacitors can rapidly discharge high currents to create a motion pulse.

Figure 4A shows a diagram of the actuation mechanism, which consists of a solenoid coil (30 × 3 turns array wound, 2.1-mm coil diameter) and a small 2.0-mm-diameter neodymium magnet. We selected the highest grade (N52) to maximize the strength of the permanent magnet. The magnet was constrained to moving up or down within a 2.1-mm-diameter tube. The tube was made of a 12.5-μm-thick polyimide film to minimize the distance between the magnet and the coil. Connecting a low series resistance capacitor to the coil results in a short, high-amplitude pulse of current, which accelerates the magnet upward, causing the structure to fold and transition as shown in Fig. 4 (B and C) and movie S6. We note that these diagrams are shown with the tube oriented upward to better illustrate the components; however, the microflier rotates in its tumbling state and falls with the tube oriented downward in its stable state.

We performed a series of benchmark experiments to characterize the force produced by the actuator itself before integration with the origami structure. As shown in fig. S4, a magnet attached to a carbon fiber rod and a flat reflector were placed in a polyimide tube with a solenoid coil at the base. The coil and tube were glued to a glass slide to keep them in place. A laser distance sensor (Keyence IA-030) shining down at the reflector and sampling at 1 kHz was used to measure the distance versus time as the magnet accelerated upward. The actuator was connected to the switch and capacitor circuit used on the origami microflier and probed with an oscilloscope (Tektronix MDO34) to measure the capacitor voltage shown in Fig. 4D. The second derivative of the distance waveform and the mass of the magnet and carbon fiber rod were used to calculate the force. To achieve maximum force with minimal weight, we evaluated a number of capacitors with different properties and plotted the peak force they produced. The same measurements were repeated $N = 5$ times for each of the capacitors shown in Fig. 4E. We began by testing a single capacitor and then proceeded to test two capacitors of the same type in parallel.

The peak value of approximately 250 mN was more than six times greater than the force required to transition the structure. The waveforms also show that our actuator can be controlled electronically and can respond within tens of milliseconds, meeting the requirement for fast motion. Figure 4E further demonstrates the ability to produce sufficiently large pulses of force to transition with only tens of milligrams required for energy storage.

Coupling this force to the structure, however, introduces additional challenges as we seek to replicate the bending required for state transition shown in movie S4. The magnet and coil must be able to push against each other. The structure creases must also be able to bend freely to transition, and, as the structure folds inward, the perimeter of the structure shrinks. To address this, we rigidly attached the magnet to the center of the origami structure with a carbon fiber rod because the center point experiences motion only in the *Z* direction. We also suspended the tube and coil above it using carbon fiber rods connected to the outer edges of the structure. The rods were rigidly glued to the top of the tube but were attached to the origami structure with flexible hinges made of 12.5-μm-thick polyimide film as shown in Fig. 4 (A and B). The rigid carbon fiber rods transferred force to the outer edges of the structure but must also be able to bend at their attachment points to accommodate folding. The magnet produced a force in the *Z* direction, whereas the rods pushed the structure inward in the *X* and *Y* directions. At a high level, our design operated similarly to an umbrella. Maximizing the force delivered to the structure requires optimizing the initial angle of the rods θ shown in Fig. 4A (see the Supplementary Methods and fig. S5).

To balance the large force required to transition the origami structure with the need for low power, we added an additional magnet as a passive method for reducing the force required by the actuator. By placing an additional permanent magnet in the tube above the coil, as soon as the magnet attached to the origami accelerates upward, it will experience an attractive force that will help pull it upward. In addition, once transitioned, the origami will remain in this state.

We measured the attractive forces between our two 2.0-mm-diameter N52 magnets empirically. To do this, we placed a polyimide tube on an approximately 3-cm-tall plastic object to create a raised platform on a precision weight scale (Sartorius QUINTIX125D-1S) to make sure that the magnets have no interaction with the scale and that metal components in the scale do not affect our measurement. We confirmed that magnetic effects do not affect the scale readings at this distance. We then placed our cylindrical magnet (magnet A, 1-mm diameter, 2-mm height, grade N52) on the plastic surface and placed the tube around it. We then glued another one of the same-size magnets (magnet B) to the end of a carbon fiber rod and lowered it through the top of the tube using a micromanipulator. We recorded the decrease in mass of magnet A to determine the attractive force caused by lowering magnet B, shown in Fig. 4F. As expected, the attractive force increased nonlinearly as the magnets approached each other. This allowed us to achieve a robust transition with less energy input to the coil. These results demonstrate a fully functional actuator compatible with solar-power harvesting that meets all of our design requirements.

Solar harvesting and wireless circuit

Programmably triggering our origami microflier to transition in mid-air requires an electronic circuit with multiple components for sensing, control, and power regulation. At the core of the circuit is a programmable microcontroller with an onboard Bluetooth radio (nRF52832, Nordic Semiconductor) that reads data from a temperature and pressure sensor (BMP384, Bosch) and can send a control command to the actuator to trigger it. We fabricated the entire circuit directly on a flexible sheet of copper-coated 12.5-μm-thick polyimide as shown in Fig. 5A. This allows for integrating the electronics directly with the origami structure (see Materials and Methods). In addition, this method enables scalable

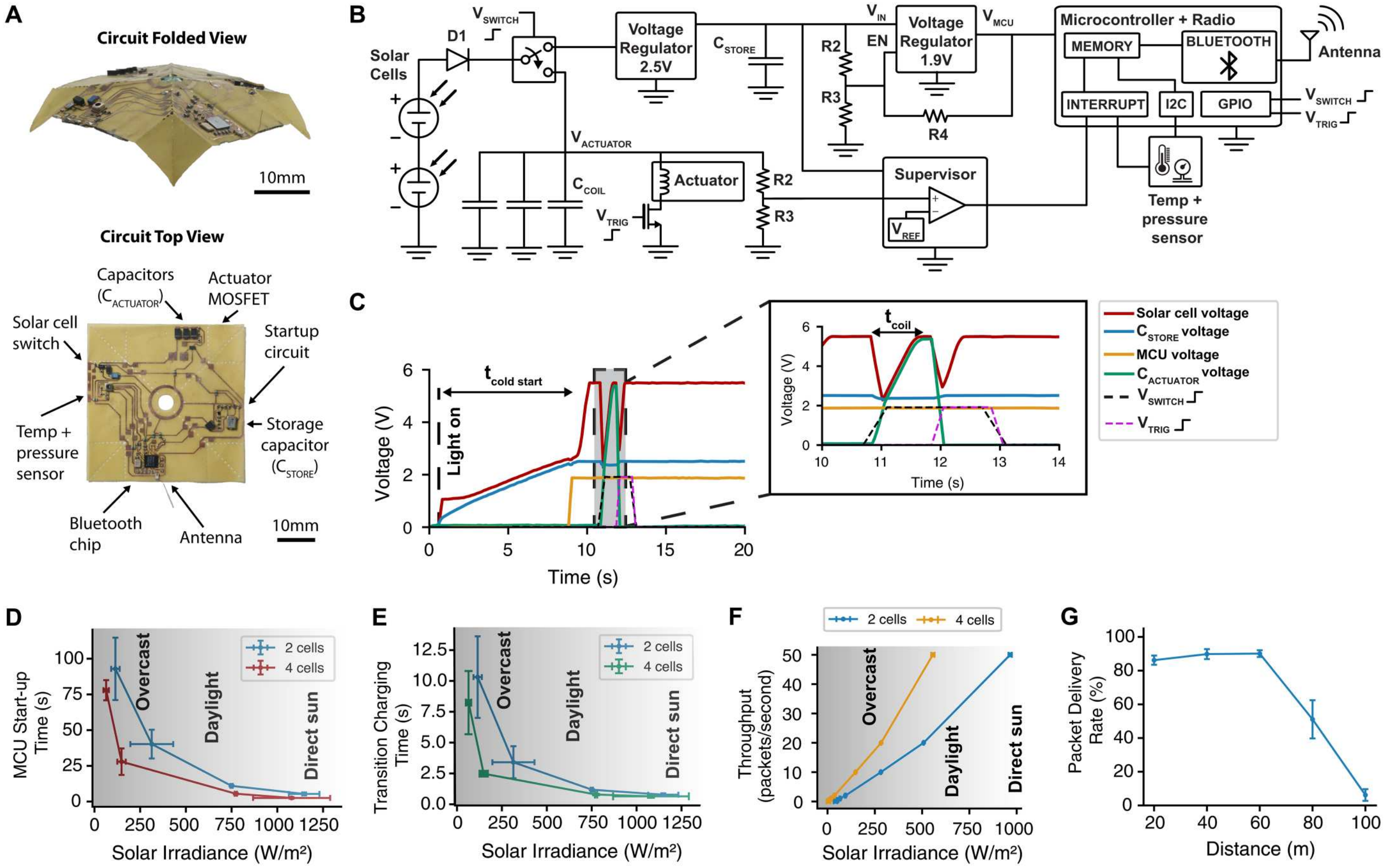

Fig. 5. Solar harvesting and wireless circuit. (**A**) Flexible circuit folded into 3D origami structure and labeled top view of major components divided into four regions for even weight distribution. (**B**) Circuit diagram showing power management for cold start, storage capacitors, and different voltage domains, as well as the wireless microcontroller and sensor. (**C**) Waveform illustrating microcontroller cold start followed by charging and triggering the actuator for transitioning the structure. (**D**) Time required to cold start the microcontroller at varying light levels ($N \geq 3$, ±σ). (**E**) Time required to charge up the capacitors to transition at varying light levels ($N \geq 3$, ±σ). (**F**) Achievable Bluetooth throughput at varying light levels ($N = 3$, ±σ). (**G**) Bluetooth packet delivery rate versus range ($N = 1000$, ±σ).

production of origami structures with integrated electronics using industry-standard circuit fabrication techniques.

Running this device with solar power, however, required addressing multiple challenges. To transition in mid-air, the solar cells must rapidly charge a lightweight energy storage element, such as a capacitor, to above 5 V for the actuator to generate a large enough force to transition our fully assembled origami microflier, as shown in Fig. 4D. However, our microcontroller could only tolerate a maximum of 3.6 V, which introduced the need for dual power regulation circuits to multiplex a single solar cell array and the ability to send control commands to these components (see the Supplementary Methods for embedded software details). In addition, to operate for extended periods of time after deployment, these devices needed to be able to cold start without any stored energy because of the lack of an onboard battery. This is challenging because many microcontrollers have short, high current power spikes when turning on. This is often due to initialization procedures, such as waiting for their clock oscillators to stabilize before they can run code to go into their low power modes.

To address these challenges, we designed the lightweight circuit shown in Fig. 5 (A and B). Power was provided to the circuit by a lightweight solar cell array. To achieve the voltage required by our actuator, we used a minimum of two solar cells (5 mm by 5 mm, Microlink Devices) connected in series. For more robust operation in low-light environments, we connected an additional two-cell array in parallel. The output of the solar cell was connected to a diode to prevent reverse current flow and then into a single pole dual throw switch. We used this switch to multiplex our solar cells between powering the microcontroller and charging the capacitors for the actuator. This strategy allowed us to rapidly charge up for transitioning using all available power and then use the power for sensing and data transmission after deployment with a single lightweight component. The switch control signal used a pull-up resistor to keep it in the default state of charging the microcontroller for startup.

To sustain the microcontroller while charging the actuator, our microcontroller needed an energy storage capacitor, C_{store}. We selected a small 7.5-mF supercapacitor that can sustain the microcontroller while transmitting Bluetooth packets at a rate of 1 packet/s for up to 1 min, even with no input power. However, this component could only tolerate a maximum of 2.6 V. We placed a voltage regulator that acted as a limiter to prevent damage. We also used a modified version of the lightweight startup circuit presented in our prior work (*4*) to enable robust cold start. Briefly, the circuit used a voltage divider from the input to trigger the enable pin of a second 1.9-V regulator when C_{store} is fully charged. Upon startup, an additional high impedance feedback path kept the system on. We also note that to achieve robust startup, we placed an additional 100-μF tantalum capacitor in parallel with the larger 7.5-mF capacitor to help buffer the initial transient power spike.

Figure 5C illustrates the full operation of the power harvesting circuit from cold start to actuation. When first exposed to light with zero charge at t_0, the microcontroller storage capacitor C_{store} begins to charge. Upon reaching 2.5 V, the voltage regulator limits the value of C_{store}, whereas the solar array increases to its maximum voltage more than 5 V. Simultaneously, the startup circuit with the 1.9-V regulator detects that C_{store} is fully charged and turns on to power the microcontroller. The time required to turn on the microcontoller, $t_{\mathrm{cold\ start}}$, was determined by the light intensity.

We evaluated the time required to charge each of the capacitors in our circuit outdoors. We placed the fully assembled origami microflier on its side with its solar cells facing up toward the sun. We connected wires between the solar cell outputs and power input to measure current with a multimeter (Fluke 289) and used 43 AWG wires connected to different points on the circuit to measure the waveforms shown in Fig. 5C using an oscilloscope (Tektronix MDO34). We placed a solar power meter (TES 132) next to the solar cells at the same angle to measure the incident solar power. We extracted the startup and charging times from the oscilloscope waveforms to generate the plots in Fig. 5D, which show the microcontroller startup time across a variety of light conditions with two and four solar cells.

The microcontroller then begins running code and can sample its sensor readings, run an onboard timer, or wait for a radio signal to determine when to transition. Figure 5C shows the circuit operating with a fixed delay, after which it set the V_{switch} signal high and began charging C_{coil}. The time required to fully charge C_{coil} also varies with light intensity. We performed measurements outdoors as explained above and plotted the results in Fig. 5E with two and four solar cells. This latency between charging and transition introduces a dependency between the available sunlight and the minimum height from which the sensors can be dropped. The circuit then waits for C_{coil} to charge, which can either be implemented with a programmed delay or using an interrupt signal from the supervisory circuit that detects when C_{coil} has reached maximum charge. Next, the circuit sets V_{trig} to high, which enables the actuator and transitions the structure.

Movie S7 shows the resulting end-to-end operation of the microflier transitioning completely untethered using solar power. In addition, movie S8 demonstrates the same end-to-end operation transitioning in mid-air when dropped outdoors from a ladder at a height of approximately 4 m. The origami microflier began falling in its tumbling state, then transitioned in mid-air to its stable state and changed its descent behavior.

After deployment, the microcontroller continued sampling its sensors. As shown in Fig. 5D, the circuit can cold start from zero charge even in low-light conditions. To understand how often our device can transmit data, we performed additional outdoor measurements to determine throughput. Because of the complexity of reprogramming the miniaturized circuit during different sun conditions, we measured the power required for Bluetooth first and then measured the power provided by the solar cells. To measure the achievable Bluetooth throughput versus light level, we programmed the microcontroller to transmit packets at different rates. We tested the maximum and minimum delays between packets allowed by the chip in its advertising mode. We powered the circuit with a source meter (Keithley 2470) and recorded the average current for a duration of 2 min. We note that shortly after startup, the circuit drew more power but then settled to a steady state after approximately 1 min. Minimal change was seen after 2 min.

To determine the light level required to achieve each transmission rate, we performed the same measurement described above using a multimeter connected between the solar cells and the circuit input during the start-up phase. We plotted the results in fig. S6 and used linear regression to generate a mapping between light level and currents. The plot shows a highly linear mapping for both two and four cells with $R^2 > 0.98$. We used these data to generate Fig. 5F. The results show that in brighter conditions, the circuit harvested enough power to transmit data at the maximum possible rate allowed by the Bluetooth radio chip, sending a packet every 20 ms.

We also evaluated the distance at which we could decode Bluetooth transmissions in outdoor environments. We evaluated Bluetooth range in an open field by placing the origami microflier on the ground in the grass and placing a receiver at increasing distances. We used the microflier's onboard antenna, a chip antenna (Johanson 2450AT14A0100) with an 8-mm length of 41 AWG wire attached to the end to improve performance (*38*–*40*) as the transmitter. For the receiver, we connected an nRF52832 development board to an 8-dBi patch antenna (L-Com, RE09P-SM) at a height of 2 m. For each trial, we transmitted $N = 1000$ packets with sequence numbers from the origami microflier and counted the number of packets correctly decoded at the receiver to determine packet delivery rate in Fig. 5G. Despite its small antenna, we observed a robust link with low packet error rates up to 60 to 70 m. This demonstrates the potential for a drone to fly over and collect data from the devices at a high altitude using a Bluetooth receiver.

Outdoor field evaluation

In addition to characterizing the components of our solar-powered origami microfliers, we performed outdoor field experiments to evaluate their real-world behavior. First, we verified that the difference in falling behavior shown in movies S1 to S3 also occurred outdoors. To evaluate this, we constructed a mechanism to drop our microfliers from a drone (DJI Mavic Mini, fig. S7). The origami microflier was placed in a compartment below the drone, and a remotely triggered servo opened the compartment. As shown in movie S9, our origami microflier was dropped from the drone at a height of 20 m. The video shows that it began falling in its tumbling state and then transitioned in mid-air to change its falling behavior to stable descent. At the beginning of its fall, the flier passed through a region affected by drone-induced airflow (*41*–*43*). We observed in movie S9 that this appeared to have minimal effect with the flier falling straight downward, potentially with some downward acceleration due to downwash. We note that the exact effects will vary with different drone configurations, and some may induce more turbulent flow in this region that could help scatter the fliers laterally.

We repeated these experiments in a range of altitudes and wind conditions as shown in movie S10 to evaluate dispersal distance. We used a hot wire anemometer sampling at a rate of 1 Hz (405i, Testo) to measure the lateral wind speed during these trials. We placed the anemometer at a fixed height of 2 m oriented in the direction that the microflier traveled because of the challenges of measuring ambient wind speed at varying altitudes and trajectories in the field. We also measured the distance from the drop location to the microflier's landing site. We combined these data to investigate the effect of lateral wind and dispersal distance seen in controlled experiments in movie S3.

Figure 6A shows a comparison of the distances traveled in tumbling and stable states versus wind speed when dropped from a height of 20 m in an open field. The data show a division between the two states, especially at higher wind speeds, confirming that the observations in movie S3 hold outdoors in higher altitudes as well.

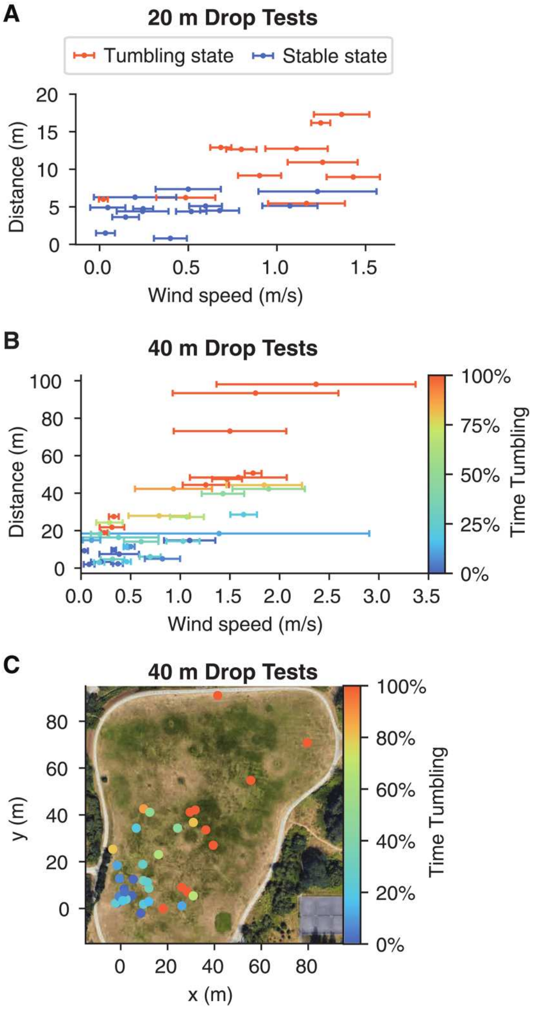

Fig. 6. Outdoor drop tests. (**A**) Outdoor drop tests from 20 m showing a comparison of distances traveled in the tumbling state and the stable state across wind conditions. $N = 24$ trials (error bars indicate ±σ, $N \geq 10$ wind measurements). (**B**) Outdoor drop tests from 40 m showing distance traveled when the microflier transitions in mid-air ($N = 38$ drop trials, error bars indicate ±σ, $N \geq 30$ wind measurements). The color bar indicates the time spent in the tumbling state before transitioning to the stable state. (**C**) Data from (B) shown as a map of landing locations, drone liftoff from (0, 0).

This is intuitively because the rotation of the sensor in the tumbling state helps maximize the area exposed to lateral wind gusts.

We also performed a series of experiments transitioning the origami microfliers in mid-air. To change the shape at different altitudes, we programmed our microfliers to transition at a fixed time delay after receiving a trigger command sent over Bluetooth. The origami microfliers were also programmed to continuously broadcast Bluetooth packets with values of their onboard counter as well as temperature and pressure readings. In our implementation, we could use the pressure sensor, a timer, or a Bluetooth command to trigger the transition. We used the same drone and wind measurement setup described above and performed drop experiments in an open park space from an altitude of 40 m. Trials were performed sequentially to facilitate recording data.

Figure 6B shows the distance traveled versus wind speed, and Fig. 6C shows the same data represented as a map of microflier landing locations. In addition, the color bar indicates the amount of time spent in the tumbling state versus the stable state. For example, 100% would indicate that the sensor was constantly tumbling and was not programmed to transition, whereas 0% would indicate that it was programmed to immediately transition and fell only in the stable state. Values between 0 and 100% indicate a mid-air transition. We observed that, similar to Fig. 6A, the longer the sensor spent in the tumbling state, the farther it traveled. Further, across microfliers that spent a similar amount of time in their tumbling state, those that experienced higher wind speeds traveled longer distances. We note that although the wind varied across our individual experiments, when dropping multiple devices programmed to transition at different times or altitudes, they will experience the same conditions and travel different relative distances. These plots demonstrate that the transitioning mechanism works in real-world environments and can achieve our goal of varied dispersal distances.

Because of their low mass and terminal velocity, our origami microfliers were not damaged by physical impact with the ground. Our design, however, requires that they land with their solar cells facing upward. To evaluate this, we performed a series of experiments dropping our origami microfliers onto a grass surface from a height of 2 m. We observed that in the tumbling state, the microfliers land upright only 52% of the time ($N = 50$). However, in their stable state, they land upright 87% of the time ($N = 50$). In the stable state, we observed that an even greater number (96%) initially landed upright but either bounced or collided with an object, causing them to flip. This shows that by transitioning to the stable state before landing, we can increase the probability of our devices landing upright to harvest power.

Figure 7A illustrates the trajectory of an origami microflier transitioning in mid-air when dropped from 15 m. Although this 2D image makes it difficult to visualize the difference in lateral distance traveled along the Y axis, the trajectory shows the device tumbling until it transitioned and stabilized in mid-air. Figure 7 (B and C) also shows data recorded from Bluetooth transmissions in real time during a drop from 50 m. Figure 7B shows the in-air sensor data as raw pressure measurements converted to altitude. The plot shows the altitude increasing as the drone lifted off and ascended to its target height of 50 m. Upon release, the microflier began to fall to the ground and showed a corresponding decrease in altitude. Figure 7C shows the temperature data from the microflier as it fell from the drone, again demonstrating the ability for the solar array to

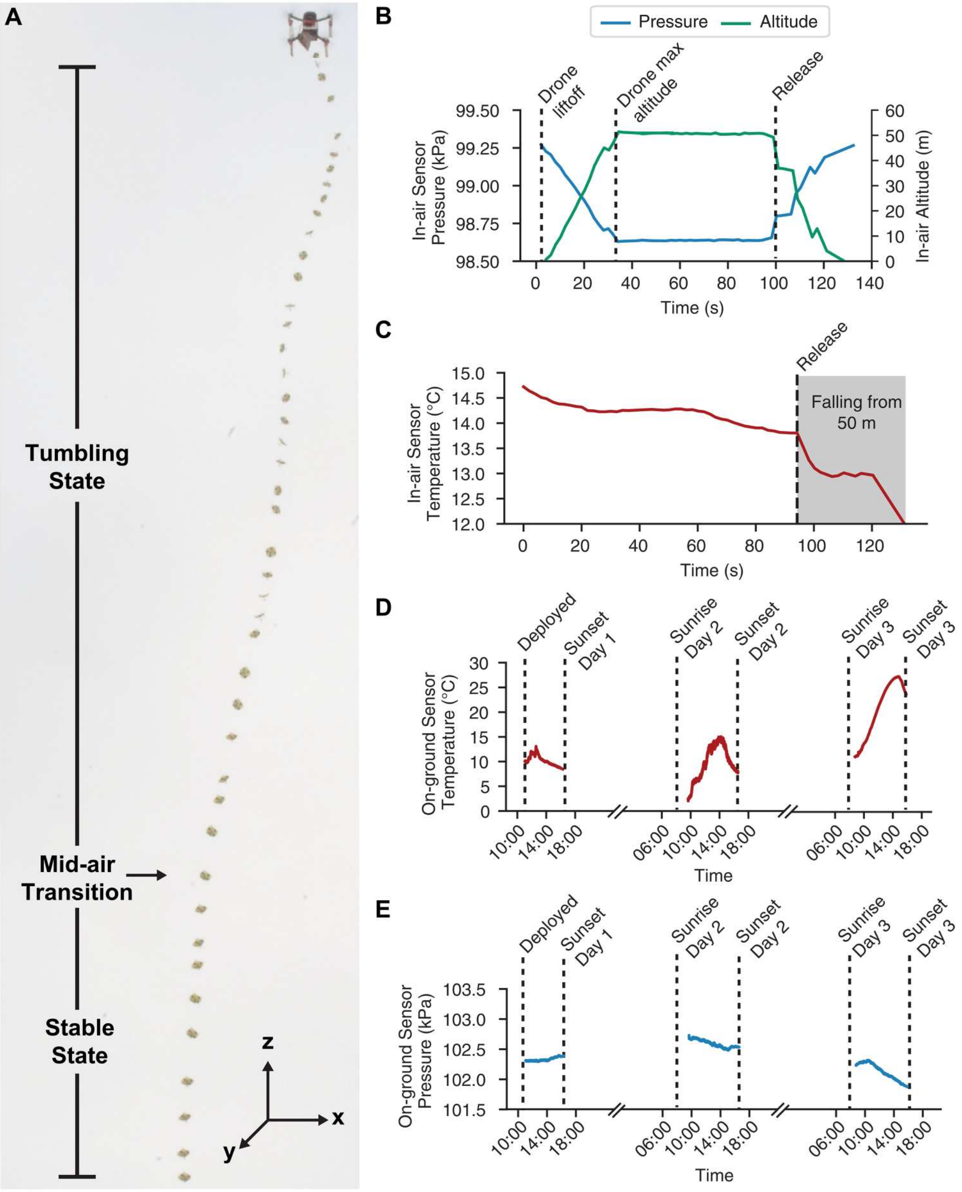

Fig. 7. In-air and on-ground microflier measurements. (**A**) Images showing our origami microflier falling from a drone and transitioning from its tumbling to stable state in mid-air. (**B**) Real-time pressure sensor readings sent via Bluetooth showing the altitude of our origami when dropped from 50 m. (**C**) Real-time temperature sensor readings sent via Bluetooth showing the temperature as our sensor falls. (**D**) Temperature readings from a 3-day outdoor deployment demonstrating that the microflier cold starts daily with harvested power. (**E**) Pressure readings from the 3-day outdoor deployment.

power our microfliers in mid-air and the potential for taking atmospheric measurements at different altitudes.

We also evaluated performance of the microflier on the ground after deployment to verify that the circuits can cold start and operate on solar power for extended periods of time. The data were collected by a computer receiving the Bluetooth measurements. Figure 7 (D and E) shows the results over the course of 3 days, during which the sensor turned off at sunset and successfully cold started shortly after sunrise. During this time, it was able to send 24,000 Bluetooth packets and operate continuously for 6 hours/day. We note that the operational time was limited by the number of sunlight hours at the deployment location in Seattle, WA in December. We performed additional measurements to evaluate sensor performance in comparison with a reference device (see the Supplementary Methods and fig. S8).

DISCUSSION

Here, we designed solar-powered origami microfliers that can change their shape in mid-air to vary their dispersal distance. Our key observation is that leaf-out origami structures exhibit distinct falling modes in their two states: a tumbling behavior conducive to wind dispersal and a stable descent state less affected by wind. We codesigned a light-weight, low-power actuator and solar power–harvesting circuit that enabled the microflier to change its shape in mid-air using solar power harvested outdoors. Our design uses a programmable microcontroller that makes it extensible to adding other sensors for a wider range of environmental monitoring applications.

Adding more payload, however, requires additional consideration to maintain a robust difference in falling behavior between the two origami states. We found that the device was sensitive to weight distribution and that adding too much weight on one unit cell could cause asymmetry and, thus, flipping in both states (see the Supplementary Methods). This can be addressed by adding balancing masses to ensure that weight is uniformly distributed across all cells. Further, the corners of our origami structures were not reinforced with carbon fiber and were flexible, which could also affect stability with larger payload.

Our origami microfliers supported bidirectional radio connectivity via Bluetooth. This allowed them to not only communicate with a base station but also potentially communicate among each other and form peer-to-peer or mesh networks. This presents multiple opportunities to both increase operational range through multi-hop communication while also presenting routing and scheduling challenges because of variability in solar power on terrains with complex geographic features (*44*). We also observed that in brighter conditions, our actuator charged fast enough to be triggered repeatedly. Modifying the design for bidirectional transitions between the states could enable more precise control over falling behavior and even motion, such as jumps, after falling to the ground. Further, our actuator, circuit, and fabrication methodology to pattern electronics directly onto the folding structure can be applied broadly to the field of origami robots, enabling a range of miniaturized battery-free designs.

Last, although our microfliers can enable field deployments of environmental sensors, we must also consider their environmental effects at their end of life and their potential to create waste. One solution is to recollect the devices after deployment. The magnets in our actuators present a means for automated collection by sweeping a magnet over the deployment area. We evaluated this using a magnetic sweeping device used to collect nails and other metallic objects on construction sites as well as a small neodymium bar magnet. As shown in fig. S9 (A to C), even these relatively small magnets can collect our microfliers from distances of 5 cm, and adding an extra onboard magnet extends this to 6 cm. These experiments demonstrate the potential for automated collection, for example, by pulling an electromagnet behind a tractor in agricultural deployments. Our onboard radio could also be used for localization and presents opportunities to use recent advances in the sensor networking communities (*45*, *46*). An alternative method that is more attractive for remote and difficult terrain would be to incorporate biodegradable materials in the design of our microfliers (*47*). Our design already eliminates batteries, and we can build on this to use biodegradable materials such as cellulose for the structural components (*34*). We hope that future advances in sustainable materials paired with innovation in microrobotic systems could enable this vision.

MATERIALS AND METHODS

Origami circuit fabrication

We fabricated our origami structures by folding sheets of polyimide films (Dupont Kapton and DuPont Pyralux AC121200E) with the pattern in Fig. 3A. We chose the number of unit cells and used a custom Python script to generate a tessellation of unit cells with the appropriate angle α. Next, we chose a film thickness and cut pattern. We tuned the structure's initial folding angle by using a small number of holes along the boundary creases and adding more cuts along the main and sub creases. The stiffer boundary crease dictated the initial folding angle and energy barrier between states. Combined, these factors determined the energy required for transition.

We used laser micromachining (LPKF U4) to cut out the shape of the origami and make the crease cuts. We chose four unit cells for our microfliers using data in Fig. 3 (D and E) and fig. S10, which indicated that this design had the highest lateral displacement, which is correlated to the greatest number of rotations during its descent and the lowest terminal velocity. In addition, this design is symmetric, which simplifies weight distribution and fabrication. We chose a side length of 39 mm based on experiments showing that smaller prototypes did not exhibit different descent behaviors. This size achieved our sub-gram target mass and provided sufficient area for the electronics.

We further demonstrated direct patterning of functional circuits onto the foldable origami to create our final microfliers shown in Fig. 2. We used a copper-coated film (12 μm of copper and 12 μm of polyimide, DuPont Pyralux AC121200E). We first covered the copper surface in an ink mask. Next, we used the laser to raster away the mask in regions around the desired pads and traces, leaving the copper exposed. We then made the crease and boundary cuts. We etched the exposed copper using ferric chloride and removed the remaining ink using acetone or isopropanol to create the final circuit. Components were then manually placed under a microscope and soldered using a hot plate at 285°C. This created a fully functional circuit on a flat, flexible sheet. This process is similar to commercial flexible circuitboard fabrication, which could be used to scale up production.

To maintain rigid origami, we attached a carbon fiber root structure as shown in Fig. 2C to reinforce the faces. We first created 110-μm-thick carbon fiber layups (0°, 45°, −45°, and 0°, Toray M46J) by laminating the layers together in a heat press (80 psi at 150°C for 90 min). We used the same laser micromachining procedure to cut out eight sections in the desired patterns matching the origami faces. We chose the root pattern to add rigidity with minimal mass. We attached the subsections of the root structure together by placing them on a piece of 50-μm-thick PET tape (Gizmo Dorks) to create a flexible hinge. The PET tape was patterned with cuts, allowing it to bend more easily and act like a hinge at the fold of the structure. This allowed for the root structures to fold at angle ψ. We attached the root structure to the leaf-out circuit in its flat state using cyanoacrylate (CA) glue. We then applied the origami folds shown in Fig. 3A to create the folded origami circuit as shown in Fig. 5A. The solar cells were placed on pieces of Kapton tape and attached to the opposite side of the structure. The solar cells (two or four 5 mm–by–5 mm cells, Microlink Devices) were manually wired together and soldered to the remainder of the circuit using 43 AWG wire.

Actuator fabrication

After creating the origami structure and circuit, we fabricated our miniaturized electromagnetic actuator and attached it to the structure. We rolled a sheet of polyimide film (12.5 μm, Dupont Kapton) into a tube (2.1-mm diameter and 10.5-mm length) to restrict the motion of the magnet. This tube was designed to match the inner diameter of our solenoid coils (2.1-mm diameter and 2.1-mm height, 30 × 3 turns array wound, Golden Eagle Coil & Plastic Ltd). We inserted the tube into the coil and used CA glue to attach it at one end of the tube. We then attached a small neodymium magnet (1.0-mm diameter and 2.0-mm height, grade N52) to a carbon fiber rod (0.25-mm diameter and 8.0-mm length) and glued it to the center of the root structure to avoid interference with the creases of the hinge. We then glued a second magnet-rod component inside the tube such that it was suspended approximately 8.0 mm above the other magnet when the structure was in its flat, tumbling state. These measurements were empirically determined from Fig. 4F and could be adjusted depending on the strength of the attractive force between the two magnets and the required transition force.

Statistical tests

Relevant uncertainties and statistical methods are noted in the corresponding figure legends.

Supplementary Materials

This PDF file includes:
Supplementary Methods
Figs. S1 to S12
References (*48–50*)

Other Supplementary Material for this manuscript includes the following:
Movies S1 to S10

REFERENCES AND NOTES

1. C. Cummins, M. Seale, A. Macente, D. Certini, E. Mastropaolo, I. M. Viola, N. Nakayama, A separated vortex ring underlies the flight of the dandelion. *Nature* **562**, 414–418 (2018).
2. D. Lentink, W. Dickson, J. L. Van Leeuwen, M. Dickinson, Leading-edge vortices elevate lift of autorotating plant seeds. *Science* **324**, 1438–1440 (2009).
3. M. Seale, A. Kiss, S. Bovio, I. M. Viola, E. Mastropaolo, A. Boudaoud, N. Nakayama, Dandelion pappus morphing is actuated by radially patterned material swelling. *Nat. Commun.* **13**, 2498 (2022).
4. V. Iyer, H. Gaensbauer, T. L. Daniel, S. Gollakota, Wind dispersal of battery-free wireless devices. *Nature* **603**, 427–433 (2022).
5. B. H. Kim, K. Li, J. T. Kim, Y. Park, H. Jang, X. Wang, Z. Xie, S. Won, H. J. Yoon, G. Lee, W. Jang, K. Lee, T. Chung, Y. H. Jung, S. Heo, Y. Lee, J. Kim, C. Tengfei, Y. Kim, J. Rogers, Three-dimensional electronic microfliers inspired by wind-dispersed seeds. *Nature* **597**, 503–510 (2021).
6. T. Helps, C. Romero, M. Taghavi, A. T. Conn, J. Rossiter, Liquid-amplified zipping actuators for micro-air vehicles with transmission-free flapping. *Sci. Robot.* **7**, eabi8189 (2022).
7. M. A. Estrada, S. Mintchev, D. L. Christensen, M. R. Cutkosky, D. Floreano, Forceful manipulation with micro air vehicles. *Sci. Robot.* **3**, eaau6903 (2018).
8. X. Zhou, X. Wen, Z. Wang, Y. Gao, H. Li, Q. Wang, T. Yang, H. Lu, Y. Cao, C. Xu, F. Gao, Swarm of micro flying robots in the wild. *Sci. Robot.* **7**, eabm5954 (2022).
9. D. J. Edwards, A. D. Kahn, S. B. Heinzen, T. Z. Young, N. J. Arnold, D. Newton, B. Eber, S. V. Carter, Cicada flying circuit board unmanned aerial vehicle, in *Proceedings of the 2018 AIAA Aerospace Sciences Meeting* (AIAA, 2018).
10. P. Pounds, S. Singh, Samara: Biologically inspired self-deploying sensor networks. *IEEE Potentials* **34**, 10–14 (2015).
11. S. Bai, Q. He, P. Chirarattananon, A bioinspired revolving-wing drone with passive attitude stability and efficient hovering flight. *Sci. Robot.* **7**, eabg5913 (2022).
12. L. Mahadevan, S. Rica, Self-organized origami. *Science* **307**, 1740 (2005).
13. H. Yasuda, K. Johnson, V. Arroyos, K. Yamaguchi, J. Raney, J. Yang, Leaf-like origami with bistability for self-adaptive grasping motions. *Soft Robot.* **9**, 938–947 (2022).
14. H. Yasuda, Z. Chen, J. Yang, Multitransformable leaf-out origami with bistable behavior. *J. Mech. Robot.* **8**, 031013 (2016).
15. R. St. Pierre, S. Bergbreiter, Toward autonomy in sub-gram terrestrial robots. *Annu. Rev. Control Robot. Auton. Syst.* **2**, 231–252 (2019).
16. S. Miyashita, S. Guitron, K. Yoshida, S. Li, D. D. Damian, D. Rus, Ingestible, controllable, and degradable origami robot for patching stomach wounds, in *Proceedings of the 2016 IEEE International Conference on Robotics and Automation (ICRA)* (IEEE, 2016), pp. 909–916.
17. S. Miyashita, S. Guitron, M. Ludersdorfer, C. R. Sung, D. Rus, An untethered miniature origami robot that self-folds, walks, swims, and degrades, in *Proceedings of the 2015 IEEE International Conference on Robotics and Automation (ICRA)* (IEEE, 2015), pp. 1490–1496.
18. G. Z. Lum, Z. Ye, X. Dong, H. Marvi, O. Erin, W. Hu, M. Sitti, Shape-programmable magnetic soft matter. *Proc. Natl. Acad. Sci. U.S.A.* **113**, E6007 (2016).
19. E. Hawkes, B. An, N. M. Benbernou, H. Tanaka, S. Kim, E. D. Demaine, D. Rus, R. J. Wood, Programmable matter by folding. *Proc. Natl. Acad. Sci. U.S.A.* **107**, 12441–12445 (2010).
20. A. Firouzeh, J. Paik, Robogami: A fully integrated low-profile robotic origami. *J. Mech. Robot.* **7**, 021009 (2015).
21. H. Shigemune, S. Maeda, Y. Hara, N. Hosoya, S. Hashimoto, Origami robot: A self-folding paper robot with an electrothermal actuator created by printing. *IEEE ASME Trans. Mechatron.* **21**, 2746–2754 (2016).
22. E. Vander Hoff, D. Jeong, K. Lee, OrigamiBot-I: A thread-actuated origami robot for manipulation and locomotion, in *Proceedings of the 2014 IEEE/RSJ International Conference on Intelligent Robots and Systems* (IEEE, 2014), pp. 1421–1426.
23. C. H. Belke, J. Paik, Mori: A modular origami robot. *IEEE ASME Trans. Mechatron.* **22**, 2153–2164 (2017).
24. K. Ma, P. Chirarattananon, S. B. Fuller, R. J. Wood, Controlled flight of a biologically inspired, insect-scale robot. *Science* **340**, 603–607 (2013).
25. J. Li, H. Godaba, Z. Zhang, C. Foo, J. Zhu, A soft active origami robot. *Extreme Mech. Lett.* **24**, 30–37 (2018).
26. Z. Zhakypov, K. Mori, K. Hosoda, J. Paik, Designing minimal and scalable insect-inspired multi-locomotion millirobots. *Nature* **571**, 381–386 (2019).
27. N. Elkunchwar, S. Chandrasekaran, V. Iyer, S. B. Fuller, Toward battery-free flight: Duty cycled recharging of small drones, in *Proceedings of the 2021 IEEE/RSJ International Conference on Intelligent Robots and Systems (IROS)* (IEEE, 2021), pp. 5234–5241.
28. H. Kobayashi, B. Kresling, J. F. V. Vincent, The geometry of unfolding tree leaves. *Proc. Biol. Sci.* **265**, 147–154 (1998).
29. M. Straubel, M. Hillebrandt, C. Hühne, Evaluation of different architectural concepts for huge deployable solar arrays for electric propelled space crafts, in *Proceedings of the 14th European Conference on Spacecraft Structures, Materials and Environmental Testing (ECSSMET)* (2016).
30. D. Focatiis, S. Guest, Deployable membranes designed from folding tree leaves. *Philos. Trans. R. Soc. A Math. Phys. Eng. Sci.* **360**, 227–238 (2002).
31. B. Hanna, J. Lund, R. Lang, S. Magleby, L. Howell, Waterbomb base: A symmetric single-vertex bistable origami mechanism. *Smart Mater. Struct.* **23**, 094009 (2014).
32. T. Tachi, Simulation of rigid origami, in *Origami 4: Fourth International Meeting of Origami Science, Mathematics, and Education* (2009).
33. D. Rus, M. T. Tolley, Design, fabrication and control of origami robots. *Nat. Rev. Mater.* **3**, 101–112 (2018).
34. F. Wiesemüller, Z. Meng, Y. Hu, A. Farinha, Y. Govdeli, P. H. Nguyen, G. Nyström, M. Kovă, Transient bio-inspired gliders with embodied humidity responsive actuators for environmental sensing. *Front. Robot. AI* **9**, 1011793 (2022).
35. J. James, V. Iyer, Y. Chukewad, S. Gollakota, S. B. Fuller, Liftoff of a 190 mg laser-powered aerial vehicle: The lightest wireless robot to fly, in *Proceedings of the IEEE International Conference on Robotics and Automation (ICRA)* (IEEE, 2018), pp. 1–8.
36. P. Bhushan, *Untethered microrobots of the rolling, jumping & flying kinds*, thesis, University of California, Berkeley (2019).
37. P. Bhushan, C. Tomlin, An insect-scale self-sufficient rolling microrobot. *IEEE Robot. Autom. Lett.* **5**, 167–172 (2020).
38. V. Iyer, M. Kim, S. Xue, A. Wang, S. Gollakota, Airdropping sensor networks from drones and insects, in *Proceedings of the 26th Annual International Conference on Mobile Computing and Networking* (2020).
39. V. Iyer, A. Najafi, J. James, S. Fuller, S. Gollakota, Wireless steerable vision for live insects and insect-scale robots. *Sci. Robot.* **5**, eabb0839 (2020).
40. V. Iyer, R. Nandakumar, A. Wang, S. B. Fuller, S. Gollakota, Living IoT: A flying wireless platform on live insects, in *Proceedings of the 25th Annual International Conference on Mobile Computing and Networking* (2019), pp. 1–15.

41. T. F. Villa, F. Salimi, K. Morton, L. Morawska, F. Gonzalez, Development and validation of a UAV based system for air pollution measurements. *Sensors* **16**, 2202 (2016).
42. D. Shukla, N. Komerath, Multirotor drone aerodynamic interaction investigation. *Drones* **2**, 43 (2018).
43. F. Yang, X. Xue, C. Cai, Z. Sun, Q. Zhou, Numerical simulation and analysis on spray drift movement of multirotor plant protection unmanned aerial vehicle. *Energies* **11**, 2399 (2018).
44. J. de Winkel, H. Tang, P. Pawełczak, Intermittently-powered bluetooth that works, in *Proceedings of the 20th Annual International Conference on Mobile Systems, Applications and Services* (2022), pp. 287–301.
45. R. Nandakumar, V. Iyer, S. Gollakota, 3D Localization for Sub-centimeter sized devices, in *Proceedings of the 16th ACM Conference on Embedded Networked Sensor Systems* (ACM, 2018), pp. 108–119.
46. R. Ayyalasomayajula, D. Vasisht, D. Bharadia, BLOC: CSI-based accurate localization for BLE Tags, in *Proceedings of the 14th International Conference on Emerging Networking EXperiments and Technologies* (2018), pp. 126–138.
47. V. Arroyos, M. L. K. Viitaniemi, N. Keehn, V. Oruganti, W. Saunders, K. Strauss, V. Iyer, B. H. Nguyen, A tale of two mice: Sustainable electronics design and prototyping, in *Proceedings of the Extended Abstracts of the 2022 CHI Conference on Human Factors in Computing Systems* (2022), pp. 1–10.
48. C. P. Bateson, A. Aliseda, Wind tunnel measurements of the preferential concentration of inertial droplets in homogeneous isotropic turbulence. *Exp. Fluids* **52**, 1373–1387 (2012).
49. Y. M. Chukewad, A. T. Singh, J. M. James, S. B. Fuller, A new robot fly design that is easier to fabricate and capable of flight and ground locomotion, in *Proceedings of the 2018 IEEE/RSJ International Conference on Intelligent Robots and Systems (IROS)* (IEEE, 2018), pp. 4875–4882.
50. M. I. Daepp, A. Cabral, V. Ranganathan, V. Iyer, S. Counts, P. Johns, A. Roseway, C. Catlett, G. Jancke, D. Gehring, *et al.*, Eclipse: An End-to-End Platform for Low-Cost, Hyperlocal Environmental Sensing in Cities, in *2022 21st ACM/IEEE International Conference on Information Processing in Sensor Networks (IPSN)* (IEEE, 2022), pp. 28–40.

Acknowledgments: We thank H. Yasuda, J. Yang, and members of the Laboratory for Engineered Materials and Structures for advice and helpful discussions on origami design. We also thank N. Sullivan for assistance with outdoor drop test experiments. **Funding:** The researchers are funded by a Moore foundation fellowship, National Science Foundation (ECCS-2054850), National GEM Consortium, Generational Google Scholar Fellowship Program, Cadence Fellowship Program, Washington NASA Space Grant Fellowship Program, and SPEEA ACE Fellowship Program. **Author contributions:** K.J. and V.A. designed and fabricated the origami structures; K.J., R.V., V.A., and V.I. fabricated circuits and actuator parts. T.E. and V.I. developed the embedded software. K.J., V.A., V.I., A.F., A.A., S.G., and S.F. designed the experiments. K.J., V.A., R.V., D.Y., A.F., A.A., and V.I. conducted experiments and characterized system performance; K.J., V.A., A.F., V.I., and D.Y. analyzed data and generated figures; V.I., K.J., A.A., and S.G. wrote the manuscript; S.G., V.I., A.A., and S.F. edited the manuscript. **Competing interests:** S.G. is a cofounder of Jeeva Wireless and Wavely Diagnostics. The other authors declare that they have no competing interests. **Data and materials availability:** All data needed to evaluate the conclusions of the paper are available in the paper or the Supplementary Materials. The data for this study have been deposited in the following database: 10.5281/zenodo.8247362. We provide design files for the microfliers as well as the microcontroller's firmware code at 10.5281/zenodo.8247362.

Submitted 22 December 2022
Accepted 17 August 2023
Published 13 September 2023
10.1126/scirobotics.adg4276

Science Robotics

Solar-powered shape-changing origami microfliers

Kyle Johnson, Vicente Arroyos, Amélie Ferran, Raul Villanueva, Dennis Yin, Tilboon Elberier, Alberto Aliseda, Sawyer Fuller, Vikram Iyer, and Shyamnath Gollakota

Sci. Robot. **8** (82), eadg4276. DOI: 10.1126/scirobotics.adg4276

Science Robotics (ISSN 2470-9476) is published by the American Association for the Advancement of Science. 1200 New York Avenue NW, Washington, DC 20005. The title *Science Robotics* is a registered trademark of AAAS.